

Understanding magnetoelectric switching in BiFeO₃ thin films

Natalya S. Fedorova^{1,*}, Dmitri E. Nikonov,² John M. Mangeri,¹ Hai Li², Ian A. Young,² and Jorge Íñiguez^{1,3,†}

¹Materials Research and Technology Department, Luxembourg Institute of Science and Technology,
5 Avenue des Hauts-Fourneaux, L-4362 Esch/Alzette, Luxembourg

²Components Research, Intel Corporation, Hillsboro, Oregon 97124, USA

³Department of Physics and Materials Science, University of Luxembourg, 41 Rue du Brill, L-4422 Belvaux, Luxembourg



(Received 28 July 2023; accepted 3 January 2024; published 12 February 2024)

In this work we use a phenomenological theory of ferroelectric switching in BiFeO₃ thin films to uncover the mechanism of the two-step process that leads to the reversal of the weak magnetization of these materials. First, we introduce a realistic model of a BiFeO₃ film, including the Landau energy of isolated domains as well as the constraints that account for the presence of the substrate and the multidomain configuration found experimentally. We use this model to obtain statistical information about the switching behavior—by running dynamical simulations based on the Landau-Khalatnikov time-evolution equation, including thermal fluctuations—and we thus identify the factors that drive the two-step polarization reversal observed in the experiments. Additionally, we apply our model to test potential strategies for optimizing the switching characteristics.

DOI: [10.1103/PhysRevB.109.085116](https://doi.org/10.1103/PhysRevB.109.085116)

I. INTRODUCTION

Magnetoelectric multiferroics are the materials that simultaneously show magnetic and ferroelectric orders. The coupling between magnetic and electric degrees of freedom enables the possibility to manipulate magnetic properties of these materials by applying an electric field and *vice versa*, which holds great potential for the development of devices with multiple functionalities and low energy consumption, as well as for their miniaturization [1,2]. Among this class of compounds, BiFeO₃ is of particular interest since it displays both ferroic orders at room temperature [3].

Below $T_C \sim 1100$ K [4,5], BiFeO₃ shows a spontaneous polarization \mathbf{P} of up to 1 C/m² aligned along a pseudocubic $\langle 111 \rangle$ direction [6,7] of its rhombohedrally distorted perovskite structure (space group $R3c$, no. 161) [8,9]. The polarization \mathbf{P} originates from the displacements of Bi³⁺ and Fe³⁺ cations with respect to O²⁻ anions, where the Bi³⁺ cations dominate since they possess stereochemically active 6s lone pairs [10,11].

At $T_N \sim 640$ K, the Fe magnetic moments in BiFeO₃ order antiferromagnetically [4,14]. The Dzyaloshinskii-Moriya (DM) interaction [15,16] drives the small canting of antialigned Fe spins which can give rise to a weak magnetization. Crucially, the DM interaction is a consequence of the symmetry breaking caused by the FeO₆ octahedral tilts of BiFeO₃ [17]. These tilts are about the axis of \mathbf{P} and are

expressed as $a^-a^-a^-$ in Glazer's notation [18]; in the following, we denote these tilts by \mathbf{R} . Indeed, the phase of the octahedral rotations defines the sign of the DM vector and, therefore, that of the weak magnetization [17]. In general, linear magnetoelectric (LME) effect is allowed by symmetry in BiFeO₃ [19,20]. However, in a bulk system, an incommensurate cycloidal spiral is superimposed on the antiferromagnetic order, which yields a zero net magnetization [21] and leads to cancellation of LME effect. Nevertheless, this cycloid can be suppressed by doping in bulk BiFeO₃ [22] or by epitaxial constraints in thin films [12,23–25]. In the cases of interest here, ferroelectricity coexists with weak ferromagnetism in BiFeO₃ at ambient conditions [7,12,17,26].

A deterministic reversal of the weak magnetization by an electric field was reported by Heron *et al.* [12] in a combined experimental and theoretical study of (001)-oriented BiFeO₃ films grown on a DyScO₃ substrate. (All the directions and plane orientations to which we refer in the text are in pseudocubic setting.) The authors demonstrated that such a magnetoelectric switching occurs as a result of a peculiar two-step polarization reversal in which a 109° rotation of \mathbf{P} is followed by a 71° rotation [see Fig. 1(f)] or *vice versa*. As it was revealed by first-principles calculations, the axis of the FeO₆ octahedral tilts rotates together with the polarization, which results in the reversal of the DM vector and, thus, the weak magnetization. Additionally, it was shown that a single step 180° \mathbf{P} switching, which does not affect FeO₆ octahedral tilts, has a significantly higher energy barrier and is therefore unfavorable. Note that such single-step \mathbf{P} switching would not result in the reversal of magnetization: indeed, the observed two-step switching path is key for magnetoelectric switching to occur in multidomain BiFeO₃ films. Additionally, it is worth noting that the magnetoelectric switching resulting from the two-step \mathbf{P} reversal is a nonperturbative effect that cannot be discussed in terms of the tensors characterizing the response to small fields.

*natalya.fedorova@list.lu

†jorge.iniguez@list.lu

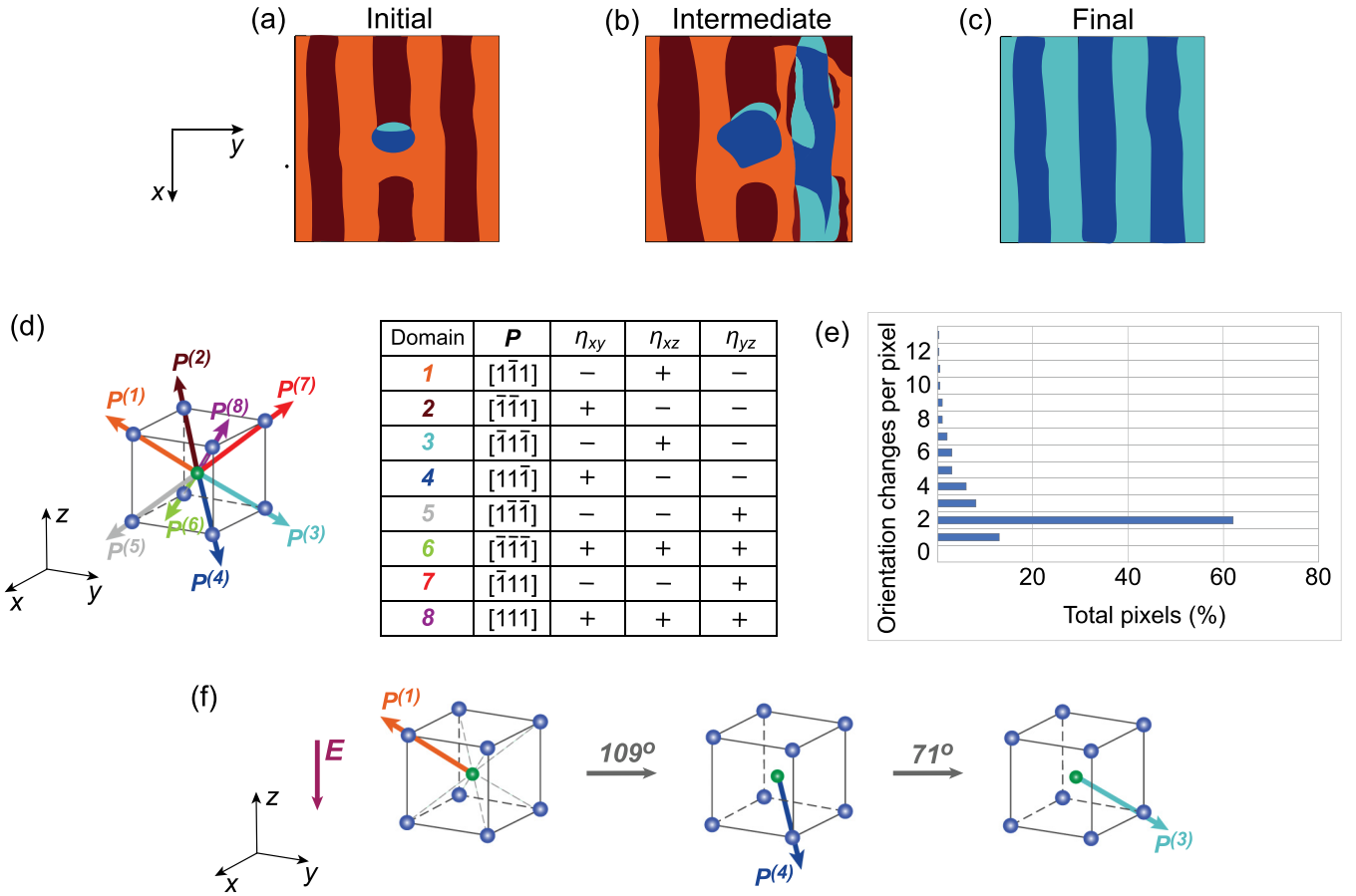


FIG. 1. Polarization switching in BiFeO₃ films grown on a DyScO₃ substrate as reported by Heron *et al.* [12]. The top row shows our hand-drawn sketches of the ferroelectric domain patterns that appear during the polarization switching process, which capture the essential features observed in the time-resolved PFM images of Refs. [12,13]. Panels (a) and (c) show the ferroelectric domain patterns in the film before and after switching, respectively, while panel (b) shows an intermediate state. Panel (d) shows the symmetry allowed polarization variants; we also list here the \mathbf{P} directions and signs of the shear strains (η_{xy} , η_{yz} , and η_{xz}) for the corresponding domains. (We use a pseudocubic setting.) Note that only the polarization variants $\mathbf{P}^{(1)}$ to $\mathbf{P}^{(4)}$ have been observed in the experiment of Heron *et al.* Panel (e) shows the number of polarization switches per pixel as obtained experimentally (data taken from Ref. [12]). Panel (f) illustrates the two-step polarization switching, with an electric field applied along $[00\bar{1}]$, where a 109° \mathbf{P} rotation is followed by a 71° \mathbf{P} rotation.

The observed possibility of manipulating a magnetization by an electric field at room temperature makes BiFeO₃ thin films very promising for designing novel magnetoelectric memory devices. However, to make them technologically relevant, the switching characteristics have to be optimized [27]. For example, in the experiments described above the applied voltages were in the range of a few volts, while the current target is to switch below 100 mV; similarly, the switching times should move from the microseconds of Ref. [12] to values in the order of 10–1000 ps [28,29]. In addition, any optimization must be compatible with maintaining the magnetoelectric control, i.e., the two-step polarization switching path has to be preserved. Therefore, to be able to optimize the switching characteristics of BiFeO₃ films, the microscopic mechanisms driving the two-step process need to be understood.

In this work, we introduce a phenomenological model of a multidomain BiFeO₃ film and investigate which physical effects (couplings) allow one to reproduce the peculiar two-step polarization reversal observed experimentally. This enables us to propose potential strategies for optimizing switching characteristics, for example, via doping.

II. PHENOMENOLOGICAL SWITCHING MODEL

A. Summary of the experimental observations

First, let us summarize the specific features of the polarization switching behavior observed in the time-resolved piezoresponse force microscopy (PFM) experiments by Heron *et al.* [12], which inform the definition of our phenomenological model.

(i) (001)-oriented films of BiFeO₃ (100 nm) with SrRuO₃ bottom electrode (8 nm) were grown on a DyScO₃ substrate to obtain a striped pattern of ferroelectric domains [30–32] with two alternating polarization directions ($\mathbf{P}^{(1)}$ and $\mathbf{P}^{(2)}$) forming 71° domain walls as illustrated in Figs. 1(a) and 1(d). The electric field was applied along the $[00\bar{1}]$ direction and it led to a 180° polarization reversal in all domains [$\mathbf{P}^{(1)}$ switched to $\mathbf{P}^{(3)}$ and $\mathbf{P}^{(2)}$ to $\mathbf{P}^{(4)}$, following the definitions in Fig. 1(d)]. The final state is shown in Fig. 1(c): it features a striped pattern of alternating $\mathbf{P}^{(3)}$ and $\mathbf{P}^{(4)}$ domains similar to that of the initial state [Fig. 1(a)]. Interestingly, only these four polarization variants occur during the switching process, out of the eight symmetry allowed possibilities shown in Fig. 1(d). Also note that, in principle, one would rather expect a 71°

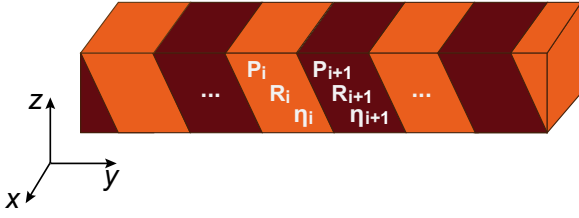


FIG. 2. Approximation of a multidomain BiFeO₃ thin film as a one-dimensional series of domains with uniform polarization \mathbf{P}_i , FeO₆ octahedral tilts \mathbf{R}_i , and strain η_i , with $i = 1, \dots, N$.

switching involving only the z component of the polarization, which is directly coupled to the electric field applied along $[00\bar{1}]$. This switching path, however, was never observed [12].

(ii) The initial and final domain configurations have the same deformation state. Indeed, all components of the strain tensor in $\mathbf{P}^{(1)}$ domains have the same magnitude and sign as those corresponding to $\mathbf{P}^{(3)}$ and the same holds for $\mathbf{P}^{(2)}$ and $\mathbf{P}^{(4)}$ domains; see Fig. 1(d) for details.

(iii) For the observed polarization variants, only domain walls (DWs) in the (011) plane satisfy the condition of charge neutrality,

$$\sigma_{\text{DW}} = (\mathbf{P}_i - \mathbf{P}_{i+1})\mathbf{n} = 0, \quad (1)$$

where σ_{DW} is the charge density at the DW, $\mathbf{n} = (0, 1, 1)/\sqrt{2}$ is the vector normal to the wall plane, and \mathbf{P}_i is the polarization of the i th domain [the domains are numbered along the y direction in Fig. 1(a); see also Fig. 2]. Otherwise, a discontinuity in the \mathbf{P} components normal to the DW plane would lead to an accumulation of bound charges, which would result in a large and unfavorable electrostatic energy penalty [33,34].

As an example, let us consider a system of two domains with the DW in the (011) plane. If the polarization in domain 1 is $\mathbf{P}^{(1)} = P(1, -1, 1)$ and $\mathbf{P}^{(2)} = P(-1, -1, 1)$ in domain 2 [see Fig. 1(d)], the charge density at the corresponding 71° DW can be computed as [Eq. (1)] $\sigma_{\text{DW},1-2} = P(2, 0, 0) \cdot (0, 1, 1)/\sqrt{2} = 0$; therefore, this DW is neutral. Similarly, $\sigma_{\text{DW}} = 0$ for (011) DWs between $\mathbf{P}^{(1)}$ and $\mathbf{P}^{(3)}$ (180° DW), as well as between $\mathbf{P}^{(1)}$ and $\mathbf{P}^{(4)}$ (109° DW) and those symmetry equivalent to them. On the other hand, the charge density at a (011) DW between $\mathbf{P}^{(1)}$ and $\mathbf{P}^{(5)}$ is $\sigma_{\text{DW},1-5} = P(0, 0, 2) \cdot (0, 1, 1)/\sqrt{2} = P\sqrt{2}$; therefore, such a DW would be charged. The same holds for (011) DWs between $\mathbf{P}^{(1)}$ and $\mathbf{P}^{(6)}$, $\mathbf{P}^{(1)}$ and $\mathbf{P}^{(7)}$, and $\mathbf{P}^{(1)}$ and $\mathbf{P}^{(8)}$, and those symmetry equivalent to them.

We thus find the following remarkable situation. Experimentally, only the $\mathbf{P}^{(1)}$, $\mathbf{P}^{(2)}$, $\mathbf{P}^{(3)}$, and $\mathbf{P}^{(4)}$ domains have been observed during the switching and it is known that the domain walls in the equilibrium multidomain states lie indeed within the (011) plane, thus being neutral [12]. This strongly suggests that the domain walls remain in the (011) plane throughout the entire ferroelectric switching. This is the situation we assume in the following.

(iv) Although 180° domain walls between $\mathbf{P}^{(1)}$ and $\mathbf{P}^{(3)}$ (or $\mathbf{P}^{(2)}$ and $\mathbf{P}^{(4)}$) would also satisfy the condition of charge neutrality described above [Eq. (1)], such boundaries have never been observed experimentally. This can be seen by monitoring the domain evolution during the switching as sketched

in Fig. 1, where the orange regions never touch the light blue regions and the brown regions are never in contact with the dark blue regions. Hence electrostatics is not the only mechanism preventing the formation of certain boundaries.

(v) More than 87% of the sample area switches in more than one step. In fact, over 60% switches in exactly two steps as shown in Fig. 1(e). The observed steps are a 109° rotation of \mathbf{P} where the y and z components are reversed (denoted as 109_{yz} switch in the following) and a 71° rotation where only the x component is reversed (71_x switch). Interestingly, the results of Refs. [12,13] suggest that the 109_{yz} switch is the nucleation event; this involves the reversal of the out-of-plane component, i.e., the one directly coupled to the applied field. Then, the 71_x switches seem related to the domain wall movements and rearrangements that occur to accommodate the switched regions and eventually yield the striped state of Fig. 1(c). Hence, in the following, we assume that the 109_{yz} events are the main driving force for the switching, while the 71_x events are a secondary effect.

B. Model of multidomain BiFeO₃ film

We now introduce a model of a multidomain BiFeO₃ film, which will allow us to identify the minimal physical ingredients that yield the observed two-step polarization switching path. For that purpose, we take into account all the features of the switching process discussed in Sec. II A.

We approximate the BiFeO₃ film as a one-dimensional series of N domains (Fig. 2), each of which is described by the uniform polarization \mathbf{P}_i , the FeO₆ antiphase octahedral tilts \mathbf{R}_i , and the strain tensor η_i . We write the total energy density of our system as

$$F = F_L + F_{\text{elec}} + F_{\text{DW}} + F_{\text{elas}}, \quad (2)$$

where F_L is the self-energy of the domains (as if they were part of an infinite unconstrained bulk material), F_{elec} is the electrostatic energy penalty associated to the formation of charged DWs, F_{DW} is the energy penalty associated to the structural discontinuity at the DWs, and F_{elas} includes the elastic constraints imposed by the DyScO₃ substrate as well as other elastic interactions affecting the domains. In the following, we describe these terms in detail.

1. Energy of bulklike domains

We define the self-energy of bulklike domains as

$$F_L = \sum_{i=1}^N F_{L,i}, \quad (3)$$

where $F_{L,i}$ is the Landau-like energy of a domain i and N is the total number of domains considered in our simulations.

Following Ref. [35], we represent $F_{L,i}$ as an expansion around the paraelectric cubic perovskite structure in powers of the electric polarization $\mathbf{P}_i = (P_{i,x}, P_{i,y}, P_{i,z})$, the FeO₆ antiphase octahedral tilts $\mathbf{R}_i = (R_{i,x}, R_{i,y}, R_{i,z})$, and the strain $\eta_i = (\eta_{i,xx}, \eta_{i,yy}, \eta_{i,zz}, \eta_{i,yz}, \eta_{i,xz}, \eta_{i,xy})$. Here $\eta_{i,xx} = \epsilon_{i,xx}$, $\eta_{i,yy} = \epsilon_{i,yy}$, $\eta_{i,zz} = \epsilon_{i,zz}$, $\eta_{i,yz} = 2\epsilon_{i,yz}$, $\eta_{i,xz} = 2\epsilon_{i,xz}$, and $\eta_{i,xy} = 2\epsilon_{i,xy}$, and $\epsilon_{i,\alpha\beta}$ are the symmetric components of the homogeneous strain tensor. The resulting expression for the

potential is written as

$$F_{L,i} = F_0 + F(\mathbf{P}_i) + F(\mathbf{R}_i) + F(\boldsymbol{\eta}_i) \\ + F(\mathbf{P}_i, \mathbf{R}_i) + F(\mathbf{P}_i, \boldsymbol{\eta}_i) + F(\mathbf{R}_i, \boldsymbol{\eta}_i), \quad (4)$$

where F_0 is the energy of the reference cubic phase of bulk BiFeO₃. $F(\mathbf{P}_i)$, $F(\mathbf{R}_i)$, and $F(\boldsymbol{\eta}_i)$ are the energy contributions due to polarization, FeO₆ tilts and strain, respectively, and have the following expressions:

$$F(\mathbf{P}_i) = A_P(P_{i,x}^2 + P_{i,y}^2 + P_{i,z}^2) \\ + B_P(P_{i,x}^2 + P_{i,y}^2 + P_{i,z}^2)^2 \\ + C_P(P_{i,x}^2 P_{i,y}^2 + P_{i,y}^2 P_{i,z}^2 + P_{i,z}^2 P_{i,x}^2), \quad (5)$$

$$F(\mathbf{R}_i) = A_R(R_{i,x}^2 + R_{i,y}^2 + R_{i,z}^2) \\ + B_R(R_{i,x}^2 + R_{i,y}^2 + R_{i,z}^2)^2 \\ + C_R(R_{i,x}^2 R_{i,y}^2 + R_{i,y}^2 R_{i,z}^2 + R_{i,z}^2 R_{i,x}^2), \quad (6)$$

and

$$F(\boldsymbol{\eta}_i) = \frac{1}{2}C_{11}(\eta_{i,xx}^2 + \eta_{i,yy}^2 + \eta_{i,zz}^2) \\ + C_{12}(\eta_{i,xx}\eta_{i,yy} + \eta_{i,yy}\eta_{i,zz} + \eta_{i,zz}\eta_{i,xx}) \\ + \frac{1}{2}C_{44}(\eta_{i,yz}^2 + \eta_{i,xz}^2 + \eta_{i,xy}^2). \quad (7)$$

Since our goal is to introduce a minimal model that captures the basic energetics of BiFeO₃, we truncate the expansion in \mathbf{P}_i and \mathbf{R}_i at the fourth order (the minimum necessary to model structural instabilities) and only include harmonic terms for $\boldsymbol{\eta}_i$. Then, $F(\mathbf{P}_i, \mathbf{R}_i)$, $F(\mathbf{P}_i, \boldsymbol{\eta}_i)$, and $F(\mathbf{R}_i, \boldsymbol{\eta}_i)$ are the coupling terms between the considered degrees of freedom:

$$F(\mathbf{P}_i, \mathbf{R}_i) = B_{PR}(P_{i,x}^2 + P_{i,y}^2 + P_{i,z}^2)(R_{i,x}^2 + R_{i,y}^2 + R_{i,z}^2) \\ + C_{PR}(P_{i,x}^2 R_{i,x}^2 + P_{i,y}^2 R_{i,y}^2 + P_{i,z}^2 R_{i,z}^2) \\ + C'_{PR}(P_{i,x}P_{i,y}R_{i,x}R_{i,y} + P_{i,y}P_{i,z}R_{i,y}R_{i,z} \\ + P_{i,z}P_{i,x}R_{i,z}R_{i,x}), \quad (8)$$

$$F(\mathbf{P}_i, \boldsymbol{\eta}_i) = \gamma_{P111}(\eta_{i,xx}P_{i,x}^2 + \eta_{i,yy}P_{i,y}^2 + \eta_{i,zz}P_{i,z}^2) \\ + \gamma_{P122}[\eta_{i,xx}(P_{i,y}^2 + P_{i,z}^2) + \eta_{i,yy}(P_{i,x}^2 + P_{i,z}^2) \\ + \eta_{i,zz}(P_{i,x}^2 + P_{i,y}^2)] \\ + \gamma_{P423}(\eta_{i,yz}P_{i,y}P_{i,z} + \eta_{i,xz}P_{i,z}P_{i,x} + \eta_{i,xy}P_{i,x}P_{i,y}), \quad (9)$$

and

$$F(\mathbf{R}_i, \boldsymbol{\eta}_i) = \gamma_{R111}(\eta_{i,xx}R_{i,x}^2 + \eta_{i,yy}R_{i,y}^2 + \eta_{i,zz}R_{i,z}^2) \\ + \gamma_{R122}[\eta_{i,xx}(R_{i,y}^2 + R_{i,z}^2) + \eta_{i,yy}(R_{i,x}^2 + R_{i,z}^2) \\ + \eta_{i,zz}(R_{i,x}^2 + R_{i,y}^2)] \\ + \gamma_{R423}(\eta_{i,yz}R_{i,y}R_{i,z} + \eta_{i,xz}R_{i,z}R_{i,x} + \eta_{i,xy}R_{i,x}R_{i,y}). \quad (10)$$

Again, for simplicity we only include in the model the lowest-order symmetry-allowed couplings.

In Eqs. (5)–(10), A , B , C , C' , and γ are the expansion coefficients that one can compute for bulk BiFeO₃ using density functional theory (DFT); see Sec. SV of the Supplemental

Material [36] and Refs. [37–40] therein. [For convenience, the coefficients C_{11} , C_{12} , and C_{44} of Eq. (7) as well as γ of Eqs. (9) and (10) are given in Voigt notation.] The values are given in Table I. This model allows one to accurately predict the energies and structural properties of BiFeO₃ polymorphs that are relevant for the purposes of studying polarization switching. Additional details on the model and the physical insights that it provides, as well as the methods for computing its parameters, can be found in Ref. [35].

2. Electrostatic energy penalty

The formation of charged domain walls gives rise to a large and unfavorable electrostatic energy penalty, which makes them unstable. Note that, in the general case, various screening mechanisms (e.g., charged defects, inhomogeneities in the polarization field) may favor the occurrence of charged DWs. However, since in the discussed experiments of Heron *et al.* [12] charged DWs were never observed, we assume that these mechanisms were not present or effective enough in the investigated samples. Therefore, for the present purposes, we disregard charged interfaces as well as all possible

	Default set	Units
A_P	−1.747	$\times 10^{-19} \text{ J m}^4 \text{ C}^{-2}$
B_P	1.070	$\times 10^{-19} \text{ J m}^8 \text{ C}^{-4}$
C_P	−7.486	$\times 10^{-20} \text{ J m}^8 \text{ C}^{-4}$
A_R	−8.555	$\times 10^{-22} \text{ J deg}^{-2}$
B_R	2.169	$\times 10^{-24} \text{ J deg}^{-4}$
C_R	−1.240	$\times 10^{-24} \text{ J deg}^{-4}$
C_{11}	1.833	$\times 10^{-17} \text{ J}$
C_{12}	7.301	$\times 10^{-18} \text{ J}$
C_{44}	4.600	$\times 10^{-18} \text{ J}$
B_{PR}	1.121	$\times 10^{-21} \text{ J m}^4 \text{ C}^{-2} \text{ deg}^{-2}$
C_{PR}	−3.437	$\times 10^{-22} \text{ J m}^4 \text{ C}^{-2} \text{ deg}^{-2}$
C'_{PR}	−2.245	$\times 10^{-21} \text{ J m}^4 \text{ C}^{-2} \text{ deg}^{-2}$
γ_{P111}	−9.444	$\times 10^{-19} \text{ J m}^4 \text{ C}^{-2}$
γ_{P122}	−1.557	$\times 10^{-19} \text{ J m}^4 \text{ C}^{-2}$
γ_{P423}	−3.232	$\times 10^{-19} \text{ J m}^4 \text{ C}^{-2}$
γ_{R111}	−1.178	$\times 10^{-21} \text{ J deg}^{-2}$
γ_{R122}	1.158	$\times 10^{-22} \text{ J deg}^{-2}$
γ_{R423}	1.155	$\times 10^{-21} \text{ J deg}^{-2}$
K_{elec}	1.602	$\times 10^{-19} \text{ J m}^4 \text{ C}^{-2}$
$K_{\text{DW},P}$	4.756	$\times 10^{-2} \text{ J m}^2 \text{ C}^{-2}$
$K_{\text{DW},R}$	4.733	$\times 10^{-4} \text{ J m}^{-2} \text{ deg}^{-2}$
$K_{\text{elas},xy}$	4.600	$\times 10^{-18} \text{ J}$
$K_{\text{elas},xz}$	4.600	$\times 10^{-18} \text{ J}$
$K_{\text{elas},yz}$	4.600	$\times 10^{-18} \text{ J}$
L_P	2.000	$\times 10^2 \text{ F m}^{-1} \text{ s}^{-1}$
L_R	8.319	$\times 10^4 \text{ deg}^2 \text{ m}^3 \text{ J}^{-1} \text{ s}^{-1}$
L_η	1.714	$\text{m}^3 \text{ J}^{-1} \text{ s}^{-1}$
Q_P	2.000	$\times 10^2 \text{ F m}^{-1} \text{ s}^{-1}$
Q_R	8.319	$\times 10^4 \text{ deg}^2 \text{ m}^3 \text{ J}^{-1} \text{ s}^{-1}$

mechanisms that can facilitate their appearance. To ensure that our model precludes charged DWs, we introduce the term

$$F_{\text{elec}} = \frac{1}{2} K_{\text{elec}} \sum_{i=1}^{N-1} |(\mathbf{P}_i - \mathbf{P}_{i+1}) \cdot \mathbf{n}|^2, \quad (11)$$

where K_{elec} is an electrostatic penalty constant. Calculating K_{elec} from first principles would require DFT simulations of charged domain walls in BiFeO₃. This, however, is very challenging due to their instability. Thus, since charged domain walls are not observed during polarization switching in the experiments of interest here, we simply assume $K_{\text{elec}} > 0$ with a magnitude large enough to prevent their formation in our simulations (see Table I).

3. Structural energy of domain walls

The next term, F_{DW} , describes the energy penalty due to structural discontinuity associated to the formation of DWs and we define it as

$$F_{\text{DW}} = F_{\text{DW},P} + F_{\text{DW},R}. \quad (12)$$

Here, the $F_{\text{DW},P}$ contribution arises from the change of the polarization across the wall and we write it as

$$F_{\text{DW},P} = \frac{1}{2} K_{\text{DW},P} \sum_{i=1}^{N-1} \sum_{\alpha=x,y,z} (P_{i,\alpha} - P_{i+1,\alpha})^2. \quad (13)$$

In turn, the $F_{\text{DW},R}$ term penalizes a discontinuity in the octahedral tilt pattern and has the form

$$F_{\text{DW},R} = \frac{1}{2} K_{\text{DW},R} \sum_{i=1}^{N-1} \sum_{\alpha=x,y,z} (R_{i,\alpha} - R_{i+1,\alpha})^2. \quad (14)$$

As one can see from Eqs. (13) and (14), the domain wall energy is minimized if polarization and octahedral tilts are uniform across the sample (i.e., for a monodomain configuration). We use the DFT domain wall energies computed for BiFeO₃ by Dieguez *et al.* [34] to estimate the parameters $K_{\text{DW},P}$ and $K_{\text{DW},R}$. Note that the obtained values (Table I) reflect the fact that the main contribution to F_{DW} is given by $F_{\text{DW},R}$ (see more details in Sec. SI of the Supplemental Material [36]).

4. Elastic constraints

We describe the elastic constraints imposed on the system as

$$F_{\text{elas}} = F_{\text{sub}} + F_{\text{matrix}}. \quad (15)$$

Here, F_{sub} takes into account the action of the DyScO₃ substrate, which forces the BiFeO₃ film to have no net shear strain in the xy plane. This leads to the formation of the experimentally observed pattern of ferroelectric and ferroelastic domains (with alternating $\mathbf{P}^{(1)}/\mathbf{P}^{(2)}$ polarization variants in the initial state and $\mathbf{P}^{(3)}/\mathbf{P}^{(4)}$ variants in the final state) where the shear $\eta_{i,xy}$ alternate sign between neighboring domains [41] [see Figs. 1(a), 1(c), and 1(d)]. To favor the observed ground state, we write F_{sub} as

$$F_{\text{sub}} = \frac{1}{2} K_{\text{elas},xy} \sum_{i=1}^{N-1} (\eta_{i,xy} + \eta_{i+1,xy})^2, \quad (16)$$

where $K_{\text{elas},xy} > 0$.

Additionally, as we mentioned in Sec. II A, it is experimentally found that the deformation state is preserved during the switching process, i.e., the domains in the initial and final state have the exact same strains. Following the discussion by Heron *et al.* [12], we hypothesize that this may result from the interaction between switching domains and the matrix of as-grown domains that are not yet switched, since the electric field is applied locally in the discussed experiments. To take this into account, we write F_{matrix} as

$$F_{\text{matrix}} = F_{\text{elas},xz} + F_{\text{elas},yz}, \quad (17)$$

where

$$F_{\text{elas},xz} = \frac{1}{2} K_{\text{elas},xz} \sum_{i=1}^N (\eta_{i,xz} - \eta_{i,xz}^{\text{ref}})^2 \quad (18)$$

and

$$F_{\text{elas},yz} = \frac{1}{2} K_{\text{elas},yz} \sum_{i=1}^N (\eta_{i,yz} - \eta_{i,yz}^{\text{ref}})^2. \quad (19)$$

Here, $\eta_{i,xz}^{\text{ref}} > 0$ ($\eta_{i,xz}^{\text{ref}} < 0$) for odd i (for even i) are the strains corresponding to the initial state or the unswitched region [see Fig. 1(d)]. In turn, $\eta_{i,yz}^{\text{ref}} < 0$ for all observed polarization variants ($\mathbf{P}^{(1)}$ to $\mathbf{P}^{(4)}$). The magnitude of $\eta_{i,xz}^{\text{ref}}$ and $\eta_{i,yz}^{\text{ref}}$ is obtained by minimizing the energy of single domain BiFeO₃ [Eq. (4)] with no applied electric field; we get $|\eta_{i,xz}^{\text{ref}}| = |\eta_{i,yz}^{\text{ref}}| = 0.0059$.

As an initial guess, we take $K_{\text{elas},xy}$, $K_{\text{elas},xz}$, and $K_{\text{elas},yz}$ equal to the elastic constant C_{44} as computed for BiFeO₃ using DFT, which captures the stiffness against a shear strain that is typical of perovskite oxides (see Table I). Note that this is a very crude approximation. For example, the energy penalty associated to the strain relaxation of the BiFeO₃ film (so it adopts its preferred shear strain and overcomes the clamping by the substrate) will be associated to the formation of misfit dislocations [42]. By contrast, the energy penalty imposed by a typical C_{44} can be expected to be much smaller. Hence, in the absence of a better quantitative guideline, the values of K_{elas} constants ($K_{\text{elas},xy}$ in particular) will play the role of adjustable parameters in our discussion.

5. Effect of domain size

In the sections above we have introduced all the terms in our model potential F . Now, to construct the total energy of a particular multidomain structure, we have to pay attention to its specific dimensions (e.g., its domain width) and how the different energy terms scale with them.

For example, the Landau energy $F_{L,i}$ and the elastic energy penalty F_{elas} scale with the domain width. By contrast, the domain wall energy F_{DW} is defined by the discontinuity in \mathbf{P} and \mathbf{R} at the wall and it is therefore independent of the domain width. Finally, the electrostatic penalty F_{elec} scales with the domain width; yet, this is not important here, since we choose K_{elec} large enough so that the formation of charged domain boundaries is fully precluded.

Thus, following experiments [12,43], let us assume that our state of interest features domains that are 100 nm wide, which is typical of BiFeO₃ films about 100 nm thick. For

simplicity, we use a domain volume $V_d = (100 \text{ nm})^3$, noting that the length of the third dimension plays no role in the problem. This would correspond to domains with about $N_{uc,d} = V_d/V_{uc} = 1.7 \times 10^7$ five-atom BiFeO₃ unit cells in them, using $V_{uc} = (0.3866 \text{ nm})^3$ for the cell volume. Similarly, we have DWs with an area $S_{DW} = (100 \text{ nm})^2$.

Now, in Table I we give the parameters $A_P, B_P, C_P, \dots, \gamma_{R423}$ to compute the domain self-energy *per unit cell* (*uc*),

$$\begin{aligned} f &= \frac{F}{V_d} - \mathbf{E} \sum_i \mathbf{P}_i = \frac{1}{V_d} (F_L + F_{\text{elec}} + F_{\text{elas}} + F_{\text{DW}}) - \mathbf{E} \sum_i \mathbf{P}_i \\ &= \frac{1}{V_{uc} N_{uc,d}} (N_{uc,d} F_{L,uc} + N_{uc,d} F_{\text{elec},uc} + N_{uc,d} F_{\text{elas},uc} + S_{\text{DW}} F_{\text{DW},ua}) - \mathbf{E} \sum_i \mathbf{P}_i \\ &= \frac{1}{V_{uc}} (F_{L,uc} + F_{\text{elec},uc} + F_{\text{elas},uc}) + \frac{1}{V_d} S_{\text{DW}} F_{\text{DW},ua} - \mathbf{E} \sum_i \mathbf{P}_i, \end{aligned} \quad (20)$$

where we introduce various unit-cell normalized energies and \mathbf{E} is an external electric field.

C. Numerical approach to finite temperature dynamics

In order to study the switching dynamics, we solve a system of Landau-Khalatnikov time-evolution equations (LKEs) of the form [44]

$$\frac{d\phi_i}{dt} = -L_\phi \frac{\partial f}{\partial \phi_i} + \theta_{\phi_i}(t), \quad (21)$$

where ϕ_i denotes the order parameters ($\mathbf{P}_i, \mathbf{R}_i$, or η_i) in domain i , t is the time, f is the energy density of Eq. (20), and L_ϕ is the kinetic coefficient that defines the rate at which an order parameter ϕ approaches its equilibrium value. The latter are chosen such that the relaxation times for all order parameters are in the range of picoseconds (see Table I). Since we are interested in studying polarization switching dynamics at room temperature, we introduce a stochastic noise $\theta_{\phi_i}(t)$ for $\phi_i = \mathbf{P}_i$ and \mathbf{R}_i that resembles thermal fluctuations of ϕ_i following Ref. [45]. $\theta_{\phi_i}(t)$ obeys a Gaussian probability distribution and is uncorrelated in time. Its autocorrelation function is

$$\langle \theta_{\phi_i}(t) \theta_{\phi_i}(t') \rangle = \frac{2k_B T Q_\phi}{V_{uc} \Delta t} \delta(t - t'), \quad (22)$$

where k_B is Boltzmann's constant, Δt is the time step used in the simulations, and Q_ϕ defines the noise amplitude and is often chosen to be equal to the kinetic coefficient L_ϕ . Hence, at each time step in the simulations, we add the noise given by

$$\theta_{\phi_i} = \sqrt{\frac{2k_B T Q_\phi}{V_{uc} \Delta t}} n, \quad (23)$$

where n is a random number out of a normal distribution $N(\mu, \sigma^2)$ with mean $\mu = 0$ and variance $\sigma^2 = 1$.

Additionally, to account for temperature-driven changes in the free energy landscape, we include a temperature dependence in the self-energy of the domains, Eq. (4). For simplicity, we modify only the terms/expressions which presumably have the strongest impact on the materials response

which we denote $F_{L,uc}$. By contrast, the parameters $K_{\text{DW},P}$ and $K_{\text{DW},R}$ in Table I allow us to compute the DW energy *per unit area* (*ua*) associated to a discontinuity in polarization or tilts, $F_{\text{DW},ua}$. Hence, to compute the total energy, we have to weight these quantities appropriately as $N_{uc,d} F_{L,uc} + S_{\text{DW}} F_{\text{DW},ua}$. More generally, we work with an energy density f (normalized by V_d) as

properties. More specifically, instead of using constant values for the coefficients A_P and A_R entering $F(\mathbf{P}_i)$ and $F(\mathbf{R}_i)$ [Eqs. (5) and (6), respectively], we define them as follows [46,47]:

$$A_\phi = A_\phi^{(0)} \frac{T_{C,\phi} - T}{T_{C,\phi}}, \quad (24)$$

where ϕ stands for \mathbf{P} or \mathbf{R} , $A_\phi^{(0)} < 0$ is the corresponding coefficient as obtained using DFT (thus, at $T = 0$ K, see Table I), $T_{C,\phi}$ is the critical temperature below which ϕ appears in BiFeO₃ (ignoring the subtleties of the structural phase transitions in this material [3], we simply choose $T_{C,P} = 1143$ K and $T_{C,R} = 1205$ K), and T is the operating temperature of interest ($T = 300$ K).

D. Adjustable parameters

As we discussed in Sec. II B, we can estimate most of the parameters of our model using DFT results. In the following, we will refer to this parameter set as the ‘‘default set’’ (the values are given in Table I). However, we need to ensure that our model reproduces the experimentally observed switching behavior of BiFeO₃ films at room temperature.

In particular, the Landau model parameters define the depth of potential wells corresponding to the states with different polarization directions and senses of the FeO₆ octahedral rotations, as well as the height of the energy barriers between these states. Therefore, these parameters determine coercive fields and switching times in our simulations. Although we introduce a finite temperature correction to the quadratic coefficients A_P and A_R of the Landau potential [Eqs. (5) and (6), respectively, as well as Eq. (24)], this might not be sufficient to reproduce the experimental switching characteristics of BiFeO₃ films. For example, we noticed that our DFT values of the Landau model parameters are generally one order of magnitude larger than those typically used in phase-field simulations of BiFeO₃ at room temperature [48,49]. Since the latter allow operating with switching voltages that are close to the experimental values, this suggests that our DFT model parameters overestimate the height of the energy barriers.

Moreover, our model does not describe the presence of defects that serve as nucleation centers and reduce energy barriers for polarization switching. Therefore, to take these effects into account, we introduce an additional parameter K in the range from 0.6 to 1 that serves as a rescaling factor for the Landau energy F_L [Eq. (4)] and the domain wall energy F_{DW} [Eq. (12)]. For the elastic constraint terms, we consider several values of $K_{\text{elas},xy} = K_{\text{elas},xz}$, while keeping $K_{\text{elas},yz}$ [Eq. (19)] fixed to the initial DFT estimate since it only penalizes the states with polarization $\mathbf{P}^{(5)}$ to $\mathbf{P}^{(8)}$ (see Fig. 1) and, as we will demonstrate below, does not play a significant role in driving the two-step polarization switching process.

Additionally, as we discussed in Sec. II C, we take into account thermal fluctuations of the order parameters by adding the stochastic noise term [Eq. (23)] in the LKEs [Eq. (21)]. Overall, thermal fluctuations allow one to overcome switching energy barriers more easily and therefore should reduce switching fields and times in our simulations. As an initial guess for the noise amplitudes, we choose $Q_\phi = L_\phi$ (default parameter set in Table I). One has to keep in mind, however, that if these noise amplitudes are too large, we may obtain spurious switches of \mathbf{P} and \mathbf{R} , which are not observed in experiments. On the other hand, as we discuss below, too small Q_ϕ values may make $71\times$ switching events too unlikely, as these are not directly driven by the applied electric field along the $[00\bar{1}]$ direction. Therefore, we consider multiple combinations of Q_P and Q_R and select those giving the best agreement with the experiment (details below, in Sec. III A).

E. Calculation details

We perform polarization switching simulations based on the model presented in Sec. II B and LKEs introduced in Sec. II C using an in-house developed code. In all simulations, the kinetic coefficients L_ϕ of LKEs are set equal to the values in Table I. We numerically solve the system of LKEs using the classic Runge-Kutta method [50]. We use a constant time step $\delta t = 40$ fs and run each simulation for $t_{\text{tot}} = 280$ ns. Unless otherwise specified, for each choice of model and simulation parameters, we perform 200 runs with different random noise to obtain statistics of the switching events.

We apply a sinusoidal electric field $E(t) = E_{\text{max}} \sin(2\omega t)$ along $[00\bar{1}]$. Following the experiments of Heron *et al.* [12], we use $\omega = 1.8$ MHz. E_{max} values are taken in the range of 100–700 MV/m as will be detailed below.

III. RESULTS

A. Validation of the model

1. Polarization switching in monodomain BiFeO₃

First, we study the simple case of monodomain bulk BiFeO₃. The energy of this system is described solely by the Landau energy term, Eq. (4). Here we use the default values of the Landau model parameters presented in Table I. Our starting configuration (before switching) is shown in Fig. 4(a) with \mathbf{P} , \mathbf{R} , and $\boldsymbol{\eta}$ obtained by minimizing the energy of the system at $T = 0$ K with no applied electric field.

We start by identifying suitable noise amplitudes for \mathbf{P} and \mathbf{R} (Q_P and Q_R , respectively). For that purpose, we analyze time evolution of the order parameters in this system at

$E = 0$ MV/m and $T = 300$ K with different Q_P and Q_R . In such conditions, the order parameters are expected to fluctuate around their initial state, but no (spontaneous) switching events should occur. We begin with the default values of the noise amplitudes, namely, $Q_P = L_P = 200 \text{ F m}^{-1} \text{ s}^{-1}$ and $Q_R = L_R = 8.319 \times 10^4 \text{ deg}^2 \text{ m}^3 \text{ J}^{-1} \text{ s}^{-1}$. We repeated this simulation keeping the same conditions 200 times in order to obtain the statistics of \mathbf{P} and \mathbf{R} behavior. We found that in most of these runs \mathbf{P} and \mathbf{R} undergo multiple stochastic switches, in contrast with what is observed in real materials. This indicates that our default values for Q_P and Q_R overestimate thermal fluctuations in monodomain BiFeO₃.

Then, we consider a set of Q_P (in the range of 100 to 200 $\text{F m}^{-1} \text{ s}^{-1}$) and Q_R (in the range of 5×10^4 to $8 \times 10^4 \text{ deg}^2 \text{ m}^3 \text{ J}^{-1} \text{ s}^{-1}$) combinations and identify optimal choices for which most of our runs ($>90\%$) do not present any spontaneous switching events. The parameter values and switching statistics are summarized in Supplemental Table S1 (see [36]).

Next, using optimal Q_P and Q_R pairs, we move to switching simulations under applied field. First, we apply $\mathbf{E} \parallel [00\bar{1}]$ with the amplitude $E_{\text{max}} = 100$ MV/m, but observe almost no switching events (see detailed statistics in Supplemental Table S2 [36]). Then we increase the field up to $E_{\text{max}} = 200$ MV/m and find that the most likely switching event is the reversal of P_z as schematically shown in Fig. 4(a), accompanied by the reversal of R_z . An example of the time evolution of \mathbf{P} and \mathbf{R} is shown in Fig. 3, for $Q_P = 140 \text{ F m}^{-1} \text{ s}^{-1}$ and $Q_R = 7 \times 10^4 \text{ deg}^2 \text{ m}^3 \text{ J}^{-1} \text{ s}^{-1}$, which give the best statistics of the switching events. More precisely, with these parameters the aforementioned switching path was found in 92.5% of the considered runs; in 2.5% there was no switching at all, while in 5% of the runs the initial reversal of P_z was followed by the reversal of additional \mathbf{P} components resulting from thermal fluctuations in the system.

Note that in this simple monodomain situation we expect to observe the switching of only the z component of \mathbf{P} (followed by the z component of \mathbf{R}), since P_z is directly coupled to $\mathbf{E} \parallel [00\bar{1}]$, and the reversal of only one component of \mathbf{P} and \mathbf{R} has the lowest energy barrier. However, as mentioned above, this switching path has never been observed in the experiments of Heron *et al.* [12]. This indicates that the *multidomain* structure must play a crucial role in determining the experimentally observed switching.

2. Polarization switching in a multidomain BiFeO₃ film

Next we study polarization switching in a multidomain BiFeO₃ film. As we mentioned in Sec. II B, we approximate it by the one-dimensional series of domains with homogeneous internal structure characterized by \mathbf{P}_i , \mathbf{R}_i , and $\boldsymbol{\eta}_i$ (Fig. 2). We start by considering the system of four domains, with two frozen and two allowed to evolve in response to applied electric field [Fig. 4(b)]. The frozen domains are necessary for reproducing the state indicated in Fig. 1(b), where the switching region coexists with parts of the sample that remain in the zero-field configuration. Note that, since we perform our simulations using periodic boundary conditions, the results do not depend on the location of the frozen domains.

The starting configuration is indicated as the state A in Fig. 4(b) and presents a pattern of alternating domains $\mathbf{P}^{(1)}$

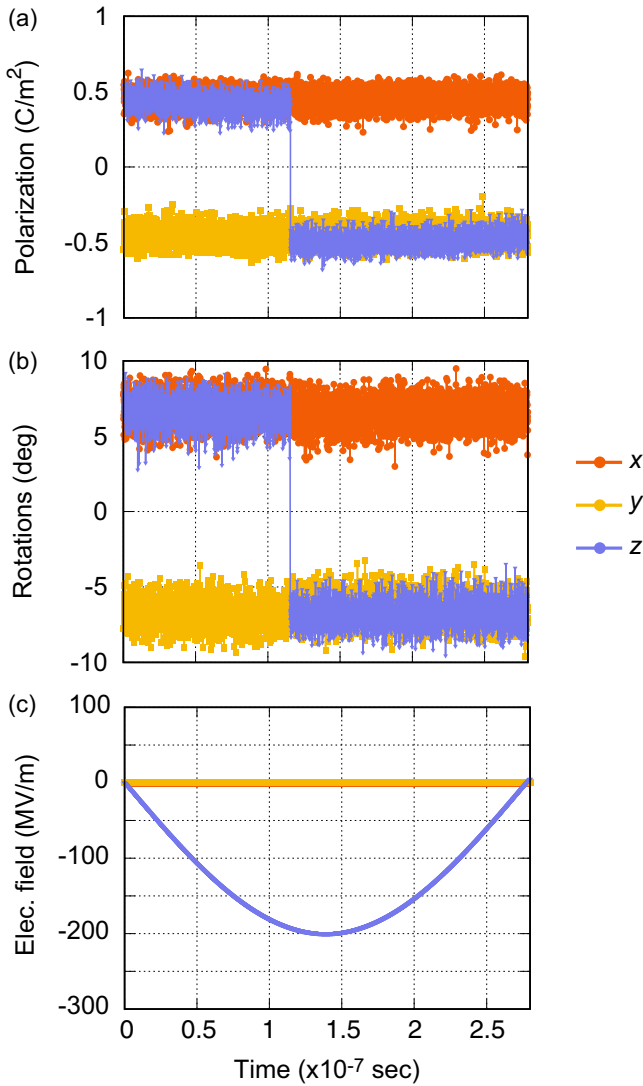


FIG. 3. Time evolution of the order parameters in monodomain bulk BiFeO_3 simulated at $T = 300$ K. We show the evolution of the polarization (a), the FeO_6 octahedral tilts (b), and the applied electric field (c).

and $\mathbf{P}^{(2)}$ reflecting the experimental situation [Fig. 1(a)]. This system is described by the full model, Eq. (2), introduced in Sec. II B, which includes the couplings related to the presence of the DyScO_3 substrate, the formation of domain walls, and the presence of the unswitched region.

First, we discuss the time evolution of \mathbf{P}_i and \mathbf{R}_i as obtained using the default model parameters presented in Table I with no rescaling ($K = 1$) and under an electric field with $E_{\text{max}} = 500$ MV/m applied along $[00\bar{1}]$ (with smaller fields, $E_{\text{max}} = 300$ and 400 MV/m , \mathbf{P}_i and \mathbf{R}_i do not switch in most of the runs). The result of one simulation (out of 200) is shown in Figs. 5(a)–5(d). One can see that the simultaneous reversal of $P_{i,y}$ and $P_{i,z}$ ($109yz$ switch) in both evolving domains is followed by the reversal of $P_{i,x}$ ($71x$ switch); further, the FeO_6 octahedral tilts reverse together with \mathbf{P}_i during this switching process. In order to better understand this behavior, let us discuss how the energy terms described in Secs. II B 2–II B 4 contribute at each step of the process.

As we have seen in Sec. III A 1, when \mathbf{E} is applied along $[00\bar{1}]$, one would expect a reversal of only the z component of the polarization, since it is the only one coupled to the field [see state C in Fig. 4(b)]. However, if this were to happen, the domain 2 would form a charged domain wall with the frozen domain 1, which is strongly penalized by the F_{elec} term in our model. The argument applies also to the domains 3 and 4. Therefore, it is preferable to perform a $109yz$ switch resulting in the state B in Fig. 4(b), which renders neutral domain walls between the switching and fixed domains. However, this state features two 180° domain walls (between the domains 1 and 2 and between 3 and 4) that have a relatively high energy on account of the terms $F_{\text{DW},P}$ and $F_{\text{DW},R}$ [Eqs. (13) and (14), respectively]. Additionally, the strain state of the B configuration is penalized by the elastic constraints F_{sub} and $F_{\text{elas},xz}$ [Eqs. (16) and (18), respectively]. Therefore, the energy can be further reduced by performing a $71x$ switch in both evolving domains, which optimizes all the energy terms in our model. This results in a full reversal of polarization in the domains 2 and 3 relative to the initial state A .

Note also that the octahedral tilts \mathbf{R}_i follow \mathbf{P}_i at each step, as there is a strong preference for \mathbf{P}_i and \mathbf{R}_i to be perfectly (anti)parallel [see the third term in Eq. (8)]. Further, there is nothing in the energetics of the tilts that tends to favor a different switching path. Hence the reversal process shown in Figs. 5(a)–5(d) is the ideal two-step ferroelectric switching path that permits an accompanying magnetoelectric reversal in BiFeO_3 .

It is important to note, however, that for the default parameter set we obtained this ideal behavior in only 5% of the runs [see Fig. 6(a)]. Additionally, in 6% of the runs we observed the perfect $109yz + 71x$ polarization reversal in only one of the evolving domains, while in the second one \mathbf{P}_i underwent either only a $109yz$ switch or did not switch at all. Nevertheless, the behavior observed in the remaining majority of runs is still physically sound. Indeed, as one can see in Fig. 6(a), in a large number of the simulations (70%) we found a $109yz + 71x$ \mathbf{P}_i reversal in at least one of the two evolving domains, followed by one or multiple backswitches of $P_{i,x}$. An illustrative example is shown in Figs. 5(e)–5(h). Here we underline that such in-plane backswitching events are unlikely to occur in real materials, which inevitably contain defects serving as pinning centers and enforcing the system to remain in the lowest-energy state. Pinning, however, is not taken into account in our simulations. For this reason, we assume that switching paths in which a $109yz + 71x$ process is followed by a series of P_x back-and-forth switches can be considered as perfect two-step switching events. Another observation is that in 21.5% of the runs we have a $71x$ first switching event in one of the domains. However, this behavior is driven by random noise. Indeed, as we will show in the following, by reducing the noise amplitudes, the number of such switching events can be dramatically reduced [see Fig. 6(b)]. The switching processes indicated in Fig. 6(a) as “Other” involve, for example, the single-step 180° polarization reversal (with or without $71x$ backswitches of \mathbf{P}_i) and $71x + 109yz$ (or just $71x$, or just $109yz$) switches in one of the domains with no \mathbf{P}_i switching in the second domain.

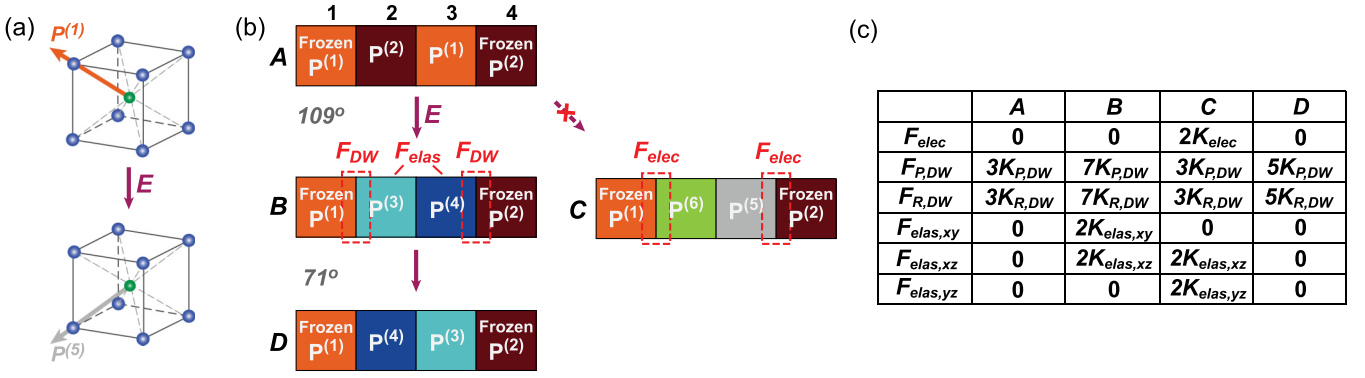


FIG. 4. Polarization switching paths that we can expect based on the model for BiFeO₃ introduced in Sec. II B. Panel (a) shows the case of monodomain bulk BiFeO₃. Panel (b) shows the case of a multidomain BiFeO₃ film, which we approximate by a system of four domains with two of them (1 and 4) frozen and two (2 and 3) allowed to evolve. Panel (c) shows the contribution from all energy terms introduced in Sec. IIB for each of the states (A to D) of panel (b); for simplicity, we do not include the couplings between the frozen domains 1 and 4 (only the couplings between the domains 1-2, 2-3 and 3-4 are taken into account). For example, state C presents two charged walls—between domains 1-2 and 3-4, respectively—and has an associated electrostatic energy penalty given by F_{elec} and labeled “ $2K_{elec}$ ” in Table I.

B. Parameter optimization

Having introduced the basic results of our simulations, we now describe how the parameters of the model can be adjusted in order to reproduce the experimental observations better.

In Table II we present seven parameter sets which we select as those giving the switching statistics closest to the experiment. These include the set that allows one to use the smallest electric field, labeled (i), the set that does not involve rescaling of the model parameters ($K = 1$), labeled (v), and the set in which all constants K_{elas} in Eqs. (16), (18), and (19) are set equal to the elastic constant C_{44} of BiFeO₃ obtained from DFT, labeled (vi). The remaining sets give a high number of two-step switches in 200 runs. In Fig. 6(c) we show the switching statistics for the representative case of set (ii), while the corresponding data for the other parameter sets are summarized in Supplemental Fig. S1 (see [36]).

One can see that by balancing the noise amplitudes and the heights of the energy barriers in the Landau potential, we can go up to 70% of two-step switching events in both evolving domains (this number goes down to 23.5% if we do not correct for spurious back-and-forth switches).

Next, we check that the observed two-step polarization switching behavior is not dependent on the small number of free domains (which is 2) used in the simulations described above. To do that, we repeat our analysis for systems of 6, 8, and 10 domains (in all cases, we freeze two domains) using the parameter sets presented in Table II. We observe a high percentage of two-step polarization reversals for all considered system sizes (details in Supplemental Figs. S2–S4 [36]). Therefore, we conclude that our minimal model of two free domains captures correctly the two-step polarization reversal.

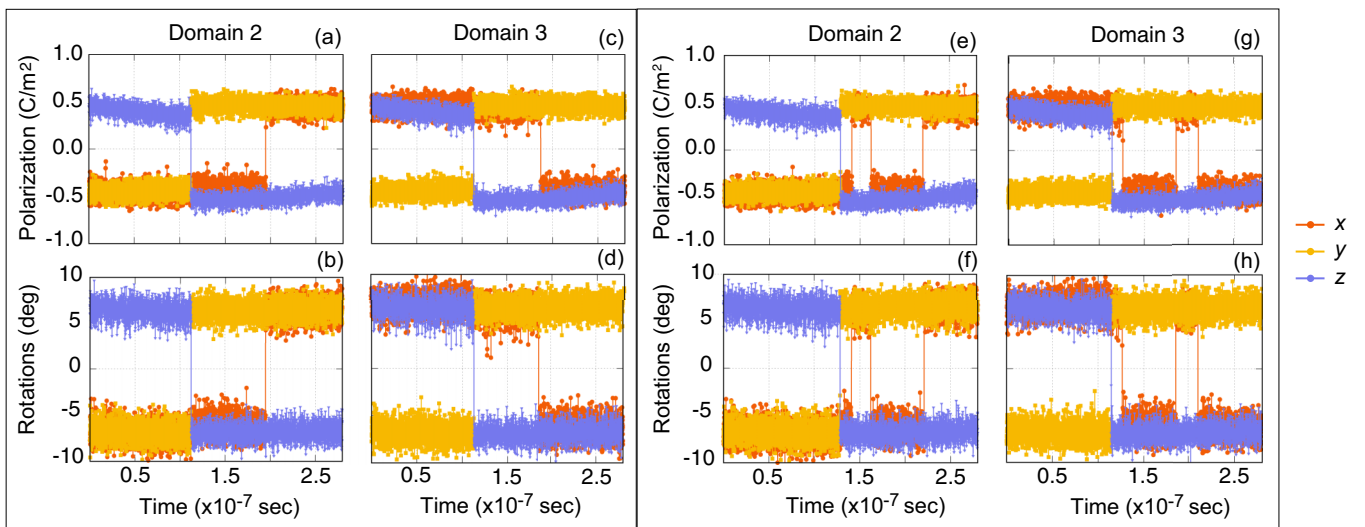


FIG. 5. Time evolution of the order parameters in BiFeO₃ simulated as a system of four domains shown in Fig. 4(b) at $T = 300$ K under an applied electric field $E_{max} = 500$ MV/m using the default parameter set (Table I). The applied electric field is time dependent as shown in Fig. 3(c). We show \mathbf{P}_i (top row) and \mathbf{R}_i (bottom row) only for the evolving domains 2 and 3. Panels (a)–(d) show the result of one of the runs (out of 200) in which we observed a perfect two-step $109y_z + 71x$ switch in both evolving domains. Panels (e)–(h) show the result of a different run where the two-step switch in both evolving domains is followed by back-and-forth switches of $P_{i,x}$ and $R_{i,x}$ (see text).

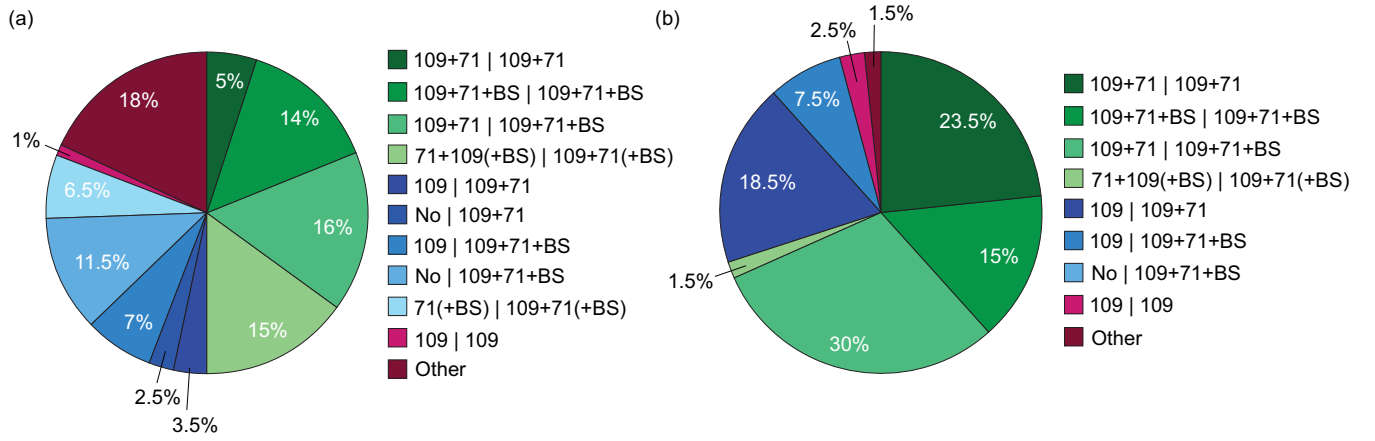


FIG. 6. Statistics of polarization switching events in the dynamical simulations of BiFeO_3 approximated by a system of four domains [two frozen and two allowed to evolve; see Fig. 4(b)]. The charts show the number of simulations (in % out of 200 runs) in which certain switching paths have been observed. Panel (a) shows the results obtained using the default parameter set in Table I, while panel (b) shows the results for the parameter set giving the highest number of $109yz + 71x$ switches [set (ii) in Table II]. “+BS” indicates the switching paths that involve backswitches of $P_{i,x}$ and $R_{i,x}$. “+(BS)” indicates that the reported number includes switching events both with and without backswitching.

C. Origin of two-step polarization reversal

In this section we analyze which terms of the model described by Eq. (2) are the key ingredients for driving two-step polarization switching in BiFeO_3 . For that we consider the system of four domains (two fixed and two free) and perform polarization switching simulations using five models of increasing complexity. Each of the considered models includes the Landau energy of the isolated domains [F_L , Eq. (3)], the electrostatic energy penalty that prevents formation of charged domain walls [F_{elec} , Eq. (11)], and the elastic energy constraint that accounts for the presence of the DyScO_3 substrate [F_{sub} , Eq. (16)]. For every model we consider the seven parameter sets presented in Table II; we perform 200 runs for each combination of model and parameter set to obtain statistics of the switching events.

We start with the model that includes only F_L , F_{elec} , and F_{sub} and perform simulations *without* freezing the domains 1 and 4; see Fig. 4(b) (note that we apply periodic boundary conditions). As one can see in Fig. 7 (model I), we mostly

obtain the $71z$ switching path similar to what we find for monodomain BiFeO_3 [Figs. 3 and 4(a)]. As already mentioned, this switching path was not observed in the experiments of Heron *et al.* [12].

Then, we freeze the domains 1 and 4 and repeat the analysis; the result is shown in Fig. 7 (model II). One can see that this immediately gives a high percentage of $109yz + 71x$ switching events. There are two main effects at play here. On the one hand, direct $71z$ switching events [which would lead to the state C shown in Fig. 4(b)] are avoided as those would result in charged domain walls with the fixed (yet-unswitched) regions. Thus we obtain the $109yz$ path instead of $71z$. On the other hand, as explained in Sec. III A 2, the substrate-imposed constraint favors the additional $71x$ jump to further optimize the energy. Hence, remarkably, this very simple model already yields the two-step polarization reversal as the dominant switching path.

Further, the ratio of the $109yz + 71x$ events can be increased by adding energy penalties for the structural discontinuity at the domain walls F_{DW} (model III in Fig. 7) and

TABLE II. Sets of model parameters giving the highest number of two-step switching events as predicted from our simulations of BiFeO_3 approximated by a system of two frozen and two evolving domains. K is the rescaling factor that we apply to our default choices for F_L and F_{DW} . $K_{\text{elas},xz}$ and $K_{\text{elas},yz}$ are the parameters of the elastic constraint terms F_{sub} and $F_{\text{elas},xz}$, respectively. Q_P and Q_R are the noise amplitudes for \mathbf{P}_i and \mathbf{R}_i , respectively. E_{max} is the amplitude of the applied electric field. N_{2d} is the number of simulations (in % out of 200 runs) in which two-step \mathbf{P}_i and \mathbf{R}_i switching occurs in both evolving domains. N_{1d} is the number of simulations (in % out of 200 runs) in which two-step \mathbf{P}_i and \mathbf{R}_i switching occurs only in one evolving domain, while in the second domain these order parameters switch only by 109° . N_{2d} and N_{1d} account for the switching events that involve back-and-forth switches of $P_{i,x}$ and $R_{i,x}$.

	i	ii	iii	iv	v	vi	vii	Units
K	0.7	0.7	0.8	0.9	1.0	0.8	0.8	
$K_{\text{elas},xy}$	32.043	160.218	48.065	48.065	160.218	4.600	160.218	$\times 10^{-18}$ J
$K_{\text{elas},xz}$	32.043	160.218	48.065	48.065	160.218	4.600	160.218	$\times 10^{-18}$ J
Q_P	1.0	1.0	1.4	1.4	1.8	1.2	1.2	$\times 10^2$ F m $^{-1}$ s $^{-1}$
Q_R	7.0	6.0	5.0	8.0	7.0	6.0	6.0	$\times 10^4$ deg 2 m 3 J $^{-1}$ s $^{-1}$
E_{max}	500	600	600	600	600	700	700	MV m $^{-1}$
N_{2d}	57	70	43	55	45	63	68.5	%
N_{1d}	33	26	44	38.5	40	28.5	25.5	%

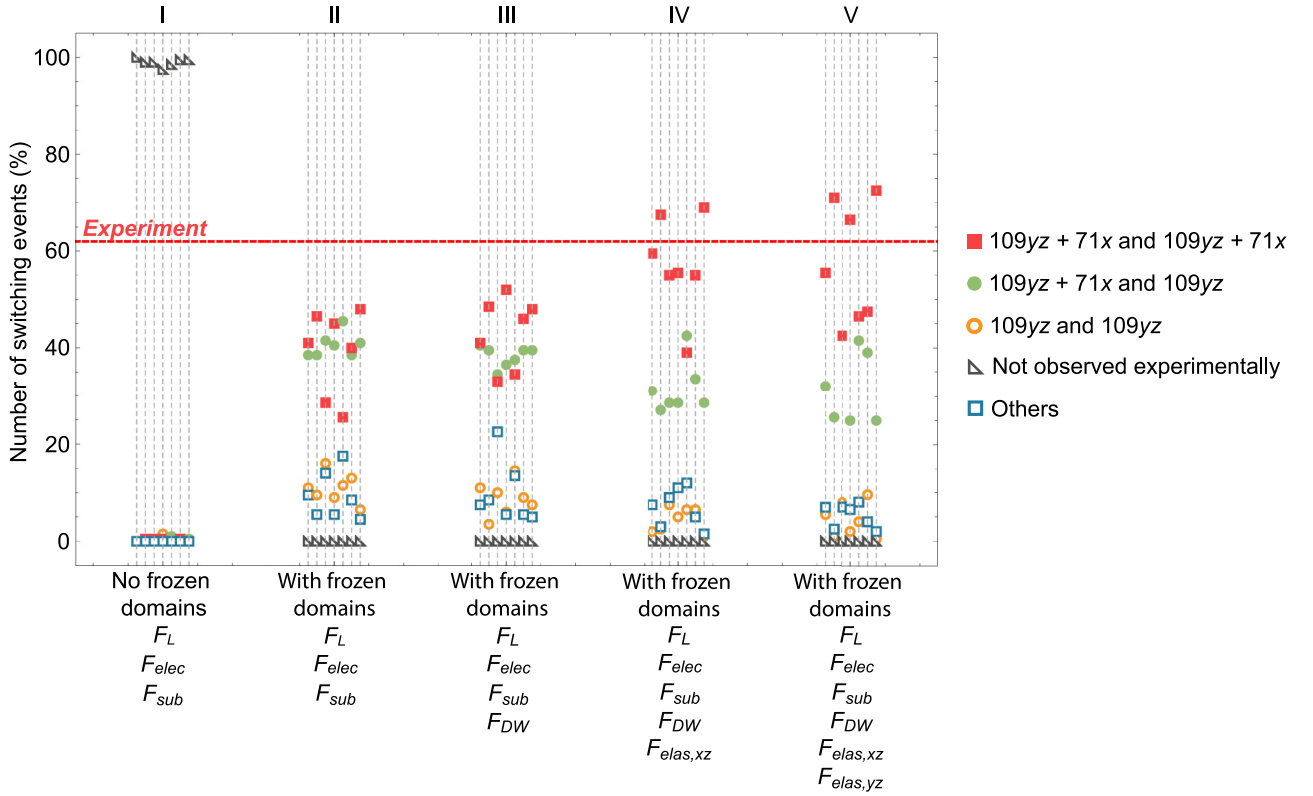


FIG. 7. Statistics of switching events for the models and simulation parameters discussed in the text. More precisely, results are presented for five models of increasing complexity. For each model we consider the seven parameter sets presented in Table II; each parameter set corresponds to a vertical dashed line. Different symbols denote different switching behaviors in domains 2 and 3. Note that the switching events indicated as $109yz + 71x$ include both perfect two-step switches as well as the paths in which the $109yz + 71x$ reversal is followed by stochastic $71x$ back-and-forth jumps. The events denoted as “Not observed experimentally” correspond to $71z$ jumps or a $109yz$ switch followed by a $71y$ rotation; such events have not been observed in the experiments of Heron *et al.* [12]. Switching events denoted as “Others” include single-step $180^\circ \mathbf{P}$ switches where \mathbf{R} does not follow, as well as switching paths that start with a $71x$ rotation. The horizontal red dashed line shows the experimentally reported fraction of the sample in which the polarization reversal occurs in two steps [12].

remaining elastic constraints (models IV and V in Fig. 7). For the latter, the addition of $F_{\text{elas},xz}$ (model IV) allows one to raise the number of two-step switches up to the experimentally reported ratio of 62%. By contrast, $F_{\text{elas},yz}$ does not play a significant role. This makes physical sense, since $F_{\text{elas},yz}$ only penalizes the switching to the domains with $\eta_{yz} > 0$ (i.e., $\mathbf{P}^{(5)}$, $\mathbf{P}^{(6)}$, $\mathbf{P}^{(7)}$, and $\mathbf{P}^{(8)}$), which are already precluded by the K_{elec} term.

IV. DISCUSSION

We have thus found that the occurrence of a two-step polarization reversal relies on three main factors: (1) the presence of a substrate enforcing the formation of the striped patterns of domains with alternating in-plane shear strains; (2) the electrostatic interactions preventing the formation of charged domain walls; (3) the presence of (yet-)unswitched regions which—in combination with point (2)—effectively preclude the direct switch of the vertical polarization component. Additionally, we find that the elastic interaction between the already switched domains and the yet-unswitched matrix ($F_{\text{elas},xz}$), as well as the energy penalty associated to the domain-wall structural discontinuity (F_{DW}), also play a role in making the two-step reversal path as dominant as observed experimentally.

A. Optimization of two-step polarization reversal

We now use our model to explore potential strategies for optimizing the switching speed and coercive field while preserving (or improving) the ratio of two-step switching events that permit magnetoelectric control of BiFeO₃ films.

These properties of interest can be tuned by modifying the parameters of the Landau energy described by Eq. (4). More precisely, we can control the amplitudes of \mathbf{P} and \mathbf{R} , as well as the switching energy barrier heights, by tuning the corresponding quadratic coefficients A_P and A_R of Eqs. (5) and (6). Additionally, we can tune the coupling between \mathbf{P} and \mathbf{R} by modifying the parameters B_{PR} , C_{PR} , and C'_{PR} of the $F(\mathbf{P}, \mathbf{R})$ term, Eq. (8).

We start by considering monodomain bulk BiFeO₃ [described solely by the Landau term, Eq. (4)] and study how changes in the model parameters A_P and A_R , as well as B_{PR} , C_{PR} , and C'_{PR} , affect the magnitude of \mathbf{P} and \mathbf{R} . First, we use the default parameter values presented in Table I and find \mathbf{P} and \mathbf{R} that minimize the energy of the system at $T = 0$ K with no applied electric field. Then we consider a series of A_P values, $A_P = \beta A_P^{\text{def}}$, where β is a number between 0.6 and 1.4 and A_P^{def} is the value of A_P in the default set. We find the equilibrium \mathbf{P} and \mathbf{R} for each considered β . As one can see in Figs. 8(a) and 8(b), increasing A_P leads to a strong

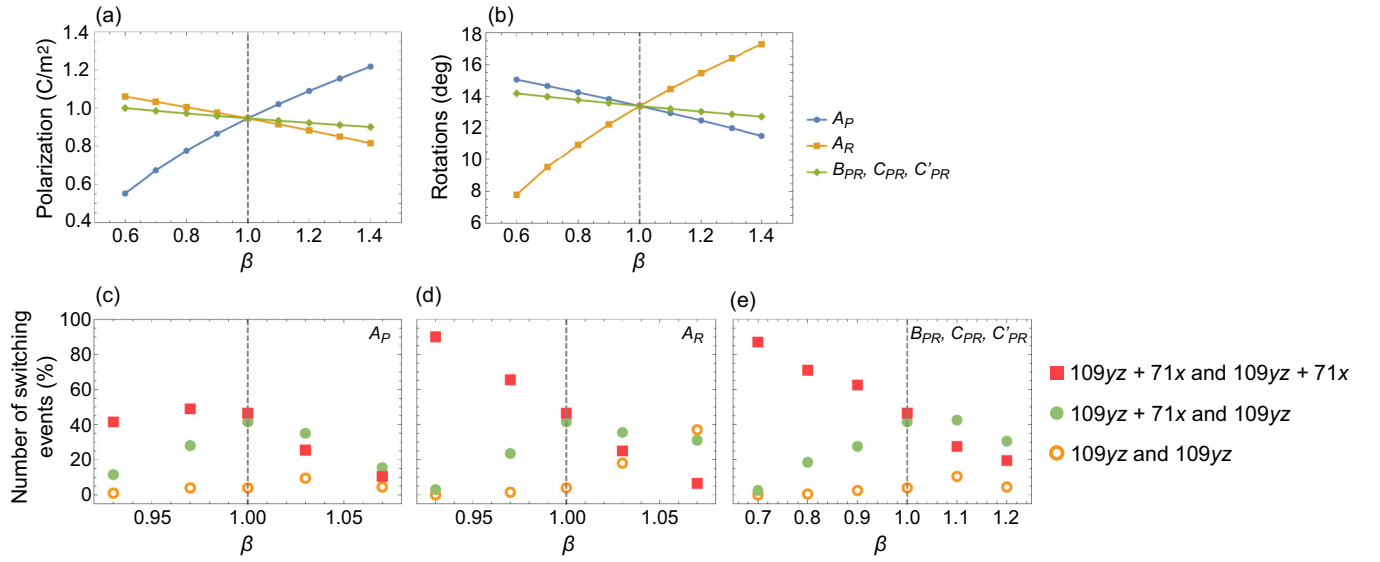


FIG. 8. Predicted changes as we vary selected parameters of our model (see text). For a given parameter X we consider $X = \beta X^{\text{def}}$, where β is a scaling factor in the range 0.6 to 1.4 and X^{def} is the value of the considered parameter from the default set. The top row shows the evolution of the magnitudes of electric polarization \mathbf{P} (a) and FeO_6 octahedral rotations \mathbf{R} (b) in monodomain BiFeO_3 . The bottom row shows the number of the switching simulations (in % out of 200 runs) in which a certain switching path has been observed in the system of four domains. Different symbols denote different switching behaviors in domains 2 and 3 (the domains 1 and 4 are frozen). Note that the switching events indicated as $109yz + 71x$ include both perfect two-step switches as well as paths in which the $109yz + 71x$ reversal is followed by $71x$ back-and-forth jumps. We show the switching statistics as we vary the A_P parameter (c), the A_R parameter (d), and the $\mathbf{P} - \mathbf{R}$ coupling parameters (e).

increase in polarization magnitude and small reduction in FeO_6 octahedral tilts. Next, we repeat the same exercise, but varying A_R . It has similar effect: increasing the magnitude of A_R causes a dramatic increase in the octahedral tilts and a small reduction of the polarization. Finally, we vary β in $B_{PR} = \beta B_{PR}^{\text{def}}$, $C_{PR} = \beta C_{PR}^{\text{def}}$, and $C'_{PR} = \beta C'_{PR}^{\text{def}}$. As shown in Figs. 8(a) and 8(b), the simultaneous scaling of all the $\mathbf{P} - \mathbf{R}$ couplings has a small effect on the magnitudes of \mathbf{P} and \mathbf{R} : we find that both decrease with increasing β .

Next, we analyze how the variation of the model parameters described above affects the switching behavior. For that purpose, we consider our minimal simulated system of four domains, two of which are frozen. We select the parameter set (v) from Table II as the starting point, since it does not involve any rescaling of the Landau energy landscape by the factor K introduced in Sec. II D.

We use this reference model to construct a series of parameter sets that differ only by the value of A_P . In particular, we define A_P as βA_P^{def} and vary β in the range of 0.7 to 1.2. For each modified set we perform 200 simulations and collect statistics of the switching events. We find that, for small A_P ($\beta < 0.9$), the local polarizations switch mostly by 180° in a single step (which can be also followed by numerous $71x$ back-and-forth jumps). At the same time, in most of these simulations the octahedral tilts do not switch at all. This makes good physical sense: as we have seen in Figs. 8(a) and 8(b), small A_P values correspond to small P_i but large R_i ; the energy barrier for reversing \mathbf{R}_i is likely too high to be overtaken via the coupling to the relatively small polarizations and it is more favorable to just reverse \mathbf{P}_i in one step (through the $P_i = 0$ state) while leaving FeO_6 octahedral tilts unaffected.

By contrast, for $\beta > 1.1$, we observe almost no switching at all, as the energy barrier is too high for the considered amplitudes of thermal noise and applied electric field. Finally, for small changes of A_P ($0.9 < \beta < 1.1$), we find that it is possible to slightly improve the ratio of two-step switching events [Fig. 8(c)]; yet, the improvement is not significant and we do not discuss it further.

Next, we repeat the same analysis for A_R . As one can see in Fig. 8(d), a small reduction of A_R yields a significant enhancement of the ratio of two-step switching events. The reason is that the reduction of A_R yields smaller R_i and smaller energy barriers for the switching of \mathbf{R}_i ; as a result, \mathbf{R}_i follows \mathbf{P}_i more easily during the electric-field-driven switching process. By contrast, an increased A_R leads to a relatively low number of $109yz + 71x$ switching events and the direct 180° polarization reversal becomes more favorable. This case is analogous to the one discussed above for a reduced A_P , which yields very stiff (unswitchable) tilts.

Thus we find that a smaller A_R yields an improved ratio of $109yz + 71x$ switching events, which suggests that this variation may also enable switching at smaller coercive fields. To check this we repeat the analysis for $\beta \leq 1$ using a maximum applied field E_{max} in the range between 500 and 600 MV/m. The obtained statistics of two-step switching events is shown in Fig. 9(a). One can see that reducing A_R indeed allows one to obtain high percentages of $109yz + 71x$ events at smaller electric fields compared to the default A_R . For example, for BiFeO_3 ($\beta = 1$) we predict that $E_{\text{max}} = 600$ MV/m is needed in order to obtain 46.5% of two-step switching events; in contrast, for a modified BiFeO_3 [e.g., a $\beta = 0.93$ in Fig. 9(a)] we obtain the same performance for $E_{\text{max}} \lesssim 550$ MV/m, which

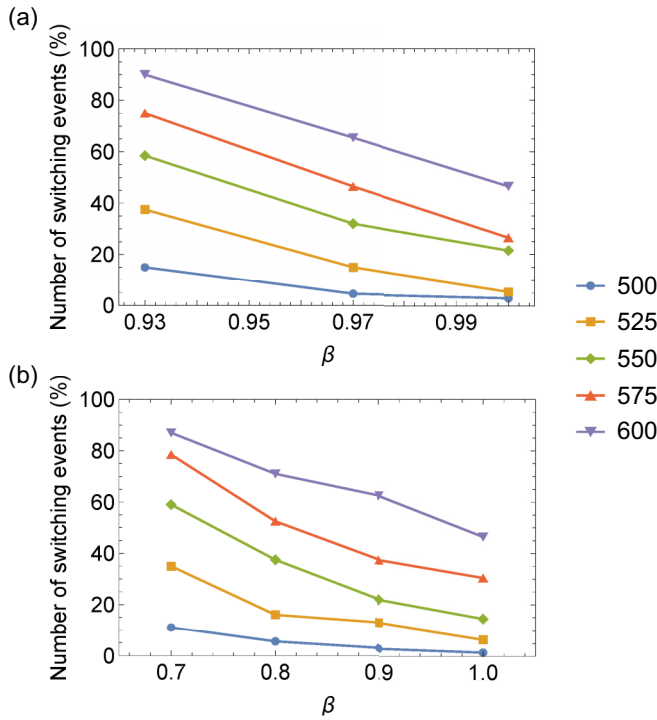


FIG. 9. Influence of the A_R parameter (a) and $\mathbf{P} - \mathbf{R}$ couplings (b) on the ratio of two-step switching events. For a given parameter X we consider $X = \beta X^{\text{def}}$, where β is a scaling factor and X^{def} is the value of the considered parameter from the default set. We show the number of the switching simulations (in % out of 200 runs) for the system of four domains (two are frozen and two are free) in which the $109y_z + 71x$ switching path has been observed in both evolving domains. The presented values include both perfect two-step switches as well as paths in which the $109y_z + 71x$ reversal is followed by back-and-forth $71x$ jumps. The different lines correspond to the different amplitudes of the maximum applied electric field (in MV/m).

amounts of an $\sim 10\%$ reduction. Therefore, this can be used as an optimization strategy for magnetoelectric switching in BiFeO_3 .

Finally, we study the effect of varying the $\mathbf{P} - \mathbf{R}$ coupling. As one can see in Fig. 8(e), we find that a reduced coupling leads to a dramatic increase in the ratio of $109y_z + 71x$ switches, since it decreases energy barriers between the states with opposite \mathbf{P}_i and \mathbf{R}_i and allows easier reversal of both degrees of freedom. Similarly to the case of varying A_R , in Fig. 9(b) we show the statistics of two-step switching events obtained using E_{\max} values from 500 to 600 MV/m. One can see that weakening the $\mathbf{P} - \mathbf{R}$ couplings in BiFeO_3 also yields a high number of $109y_z + 71x$ events at smaller E_{\max} ; therefore, it can serve as an efficient strategy for optimizing switching.

Based on our findings described above, we can suggest experimental ways to optimize magnetoelectric switching in BiFeO_3 films. As we have seen, the largest improvement of the ratio of two-step switching events is achieved by either weakening the FeO_6 tilts or by weakening the $\mathbf{P} - \mathbf{R}$ couplings. The former can be achieved experimentally, for example, by creating a solid solution of BiFeO_3 with PbTiO_3 , as the latter has a large polarization, but does not present

tilts of TiO_6 octahedra. Tuning the coupling between \mathbf{P} and \mathbf{R} might be more challenging, but we can propose some educated guesses. It is well known that \mathbf{P} in BiFeO_3 mainly originates from the displacements of the Bi^{3+} cations, due to the presence of stereochemically active $6s$ lone pairs [10,11]. Moreover, the large FeO_6 octahedral tilts in BiFeO_3 are mainly driven by the same kind of chemical mechanism, as the tilts also yield a reduced number of strong Bi-O bonds. Having the same chemical origin, it is not surprising that polarization and octahedral tilts compete strongly in BiFeO_3 , as they involve alternative ways of satisfying Bi^{3+} 's tendency to bond with a reduced number of surrounding oxygens. Therefore, this suggests that weaker $\mathbf{P} - \mathbf{R}$ couplings can be obtained by doping BiFeO_3 such that the polarization is less strongly connected to Bi^{3+} and, instead, more dependent on the off-centering of the B-site cation. This logic suggests that a solid solution of BiFeO_3 and BaTiO_3 (or any other perovskite whose polarization is strongly B-site driven) might have the desired effect.

It is important to ensure, however, that a selected optimization strategy will not be detrimental to the weak magnetization \mathbf{M} . As it has been mentioned above (and also shown in Ref. [17]), \mathbf{M} is enabled in BiFeO_3 by the symmetry breaking caused by the FeO_6 octahedral tilts; therefore, it is crucial to ensure that the tilts are not fully suppressed by doping or alloying. To appreciate by how much \mathbf{R} can be reduced without affecting significantly the magnitude of \mathbf{M} , we can refer to the recent experimental study by Karpinsky *et al.*, who investigated the structural and magnetic properties of $(1-x)\text{BiFeO}_3-x\text{BaTiO}_3$ solid solutions [51]. These authors showed that the solid solution with $x = 0.2$ presents a 20% reduction of \mathbf{R} compared to pure BiFeO_3 , while displaying $\mathbf{M} = 0.3$ emu/g at room temperature. A further reduction of \mathbf{R} (by 48% for $x = 0.25$ or more), however, leads to a reduction of the weak magnetization down to 0.02 emu/g. In this section, we have considered changes in the tilt magnitude up to 20% [see Figs. 8(c)–8(e)]; according to Ref. [51], this should be compatible with preserving a robust magnetization in the material.

In summary, we conclude that it should be possible to optimize two-step magnetoelectric switching by doping BiFeO_3 in a way that weakens either the octahedral tilts or the coupling between polarization and tilts. Interestingly, solid solutions with well-known perovskites like BaTiO_3 and PbTiO_3 appear as good candidates for this.

B. Limitations of the model

As we demonstrated in the previous section, our simple model allows reproducing experimentally observed two-step polarization switching behavior and predicting strategies for its optimization in BiFeO_3 thin films. Nevertheless, it is important to bear in mind the drastic approximations our treatment relies on and its corresponding limitations.

First, the introduced model is not universal. In fact, it describes a specific case of BiFeO_3 film grown in certain conditions (substrate, growth direction, and film thickness) [12] and having the striped domain pattern discussed above. Predicting switching behavior in BiFeO_3 films having different domain configurations or grown on substrates

imposing different elastic constraints would require adapting our simple model in ways that may not be trivial (or possible).

Second, our model is unable to reproduce the $71x$ polarization rotation being the first step in the switching, though a high number of these events have been reported by Heron *et al.* [12]. As we briefly mentioned in Sec. II A, such $71x$ \mathbf{P} rotations seem related to the movement of the domain walls, which is in turn the result of how neighboring domains rearrange during the transformation. In the simulations described above, each domain was considered as having uniform \mathbf{P}_i , \mathbf{R}_i , and η_i and, therefore, they could not capture this behavior. We tried to address this issue by considering larger domains with an inhomogeneous internal structure (see details in Supplemental Sec. SIV [36]). However, we were still unable to reproduce the experimentally observed fraction of $71x$ polarization rotations as the leading switching event.

Finally, our model is too simple to predict coercive fields accurately, for multiple reasons. First, we impose by hand a nonswitching matrix (i.e., frozen domains), a hard constraint that should result in an exaggerated coercivity. Additionally, our model does not take into account the presence of defects that usually facilitate switching by providing nucleation centers. Having said this, we think it is justified to use our model and analysis strategy in order to discuss *relative changes* (trends) of coercive fields as we vary the model parameters, elastic constraints, etc. We thus restrict our conclusions to such qualitative considerations.

V. CONCLUSIONS

In summary, in this article we discuss the model that captures the peculiar two-step polarization switching that enables an electric reversal of the magnetization in BiFeO_3 thin films. We demonstrate that the key ingredients that drive this switching process are the presence of a squarelike substrate (like DyScO_3) that enforces the formation of a striped domain pattern in the films, as well as the electrostatic interactions that prevent the occurrence of charged domain walls during the switching process. We use our model to explore strategies for optimizing the switching, i.e., to reduce the coercive fields while preserving the dominant two-step polarization reversal that enables magnetoelectric control. We conclude that (and explain why) solid solutions of BiFeO_3 with simple ferroelectric perovskites like BaTiO_3 or PbTiO_3 may be the most interesting options to explore.

ACKNOWLEDGMENTS

This work is funded by the Semiconductor Research Corporation and Intel via Contract No. 2018-IN-2865 (N.S.F. and J.Í.). We also acknowledge the support of the Luxembourg National Research Fund (Grant No. C21/MS/15799044/FERRODYNAMICS; J.Í.) and the European Union's Horizon 2020 Research and Innovation Programme (Marie Skłodowska-Curie Grant Agreement No. SCALES-897614; J.M.M.). D.E.N. worked on this project while affiliated with Intel Corp.

-
- [1] N. A. Spaldin and M. Fiebig, *Science* **309**, 391 (2005).
 [2] M. Fiebig, T. Lottermoser, D. Meier, and M. Trassin, *Nat. Rev. Mater.* **1**, 16046 (2016).
 [3] G. Catalan and J. F. Scott, *Adv. Mater.* **21**, 2463 (2009).
 [4] J. Moreau, C. Michel, R. Gerson, and W. James, *J. Phys. Chem. Solids* **32**, 1315 (1971).
 [5] R. T. Smith, G. D. Achenbach, R. Gerson, and W. J. James, *J. Appl. Phys.* **39**, 70 (1968).
 [6] D. Lebeugle, D. Colson, A. Forget, and M. Viret, *Appl. Phys. Lett.* **91**, 022907 (2007).
 [7] J. Wang, J. B. Neaton, H. Zheng, V. Nagarajan, S. B. Ogale, B. Liu, D. Viehland, V. Vaithyanathan, D. G. Schlom, U. V. Waghmare *et al.*, *Science* **299**, 1719 (2003).
 [8] C. Michel, J.-M. Moreau, G. D. Achenbach, R. Gerson, and W. James, *Solid State Commun.* **7**, 701 (1969).
 [9] F. Kubel and H. Schmid, *Acta Cryst. B* **46**, 698 (1990).
 [10] R. Seshadri and N. A. Hill, *Chem. Mater.* **13**, 2892 (2001).
 [11] O. Diéguez, O. E. González-Vázquez, J. C. Wojdeł, and J. Íñiguez, *Phys. Rev. B* **83**, 094105 (2011).
 [12] J. T. Heron, J. L. Bosse, Q. He, Y. Gao, M. Trassin, L. Ye, J. D. Clarkson, C. Wang, J. Liu, S. Salahuddin *et al.*, *Nature (London)* **516**, 370 (2014).
 [13] J. L. Bosse, L. Ye, and B. D. Huey (private communication).
 [14] V. Bhide and M. Multani, *Solid State Commun.* **3**, 271 (1965).
 [15] I. Dzyaloshinsky, *J. Phys. Chem. Solids* **4**, 241 (1958).
 [16] T. Moriya, *Phys. Rev.* **120**, 91 (1960).
 [17] C. Ederer and N. A. Spaldin, *Phys. Rev. B* **71**, 060401(R) (2005).
 [18] A. M. Glazer, *Acta Cryst. B* **28**, 3384 (1972).
 [19] Y. F. Popov, A. K. Zvezdin, G. P. Vorob'ev, A. M. Kadomtseva, V. A. Murashev, and D. N. Rakov, *Zh. Eksp. Teor. Fiz.* **57**, 65 (1993) [*JETP Lett.* **57**, 69 (1993)].
 [20] J. C. Wojdeł and J. Íñiguez, *Phys. Rev. Lett.* **103**, 267205 (2009).
 [21] I. Sosnowska, T. P. Neumaier, and E. Steichele, *J. Phys. C* **15**, 4835 (1982).
 [22] I. Sosnowska, W. Schäfer, W. Kockelmann, K. H. Andersen, and I. O. Troyanchuk, *Appl. Phys. A* **74**, s1040 (2002).
 [23] F. Bai, J. Wang, M. Wuttig, J. Li, N. Wang, A. P. Pyatakov, A. K. Zvezdin, L. E. Cross, and D. Viehland, *Appl. Phys. Lett.* **86**, 032511 (2005).
 [24] H. Béa, M. Bibes, S. Petit, J. Kreisel, and A. Barthélémy, *Philos. Mag. Lett.* **87**, 165 (2007).
 [25] D. Sando, A. Agbelele, D. Rahmedov, J. Liu, P. Rovillain, C. Toulouse, I. C. Infante, A. P. Pyatakov, S. Fusil, E. Jacquet *et al.*, *Nat. Mater.* **12**, 641 (2013).
 [26] W. Eerenstein, F. D. Morrison, J. Dho, M. G. Blamire, J. F. Scott, and N. D. Mathur, *Science* **307**, 1203 (2005).
 [27] S. Manipatruni, D. E. Nikonov, C.-C. Lin, T. A. Gosavi, H. Liu, B. Prasad, Y.-L. Huang, E. Bonturim, R. Ramesh, and I. A. Young, *Nature (London)* **565**, 35 (2019).
 [28] S. Manipatruni, D. E. Nikonov, and I. A. Young, *Nat. Phys.* **14**, 338 (2018).
 [29] B. Prasad, Y.-L. Huang, R. V. Chopdekar, Z. Chen, J. Steffes, S. Das, Q. Li, M. Yang, C.-C. Lin, T. Gosavi *et al.*, *Adv. Mater.* **32**, 2001943 (2020).

- [30] S. K. Streiffer, C. B. Parker, A. E. Romanov, M. J. Lefevre, L. Zhao, J. S. Speck, W. Pompe, C. M. Foster, and G. R. Bai, *J. Appl. Phys.* **83**, 2742 (1998).
- [31] J. X. Zhang, Y. L. Li, S. Choudhury, L. Q. Chen, Y. H. Chu, F. Zavaliche, M. P. Cruz, R. Ramesh, and Q. X. Jia, *J. Appl. Phys.* **103**, 094111 (2008).
- [32] Y.-H. Chu, Q. He, C.-H. Yang, P. Yu, L. W. Martin, P. Shafer, and R. Ramesh, *Nano Lett.* **9**, 1726 (2009).
- [33] X. Wu and D. Vanderbilt, *Phys. Rev. B* **73**, 020103(R) (2006).
- [34] O. Diéguez, P. Aguado-Puente, J. Junquera, and J. Íñiguez, *Phys. Rev. B* **87**, 024102 (2013).
- [35] N. S. Fedorova, D. E. Nikonov, H. Li, I. A. Young, and J. Íñiguez, *Phys. Rev. B* **106**, 165122 (2022).
- [36] See Supplemental Material at <http://link.aps.org/supplemental/10.1103/PhysRevB.109.085116> for details of the calculations of the model parameters (in particular, for the term describing the energy of bulklike domains as well as for the term describing the structural energy of domain walls), statistics of the switching simulations for monodomain and multidomain BiFeO₃ for different amplitudes of thermal noise on polarization and FeO₆ octahedral tilts, and different amplitudes of an applied electric field.
- [37] G. Kresse and J. Furthmüller, *Phys. Rev. B* **54**, 11169 (1996).
- [38] J. P. Perdew, A. Ruzsinszky, G. I. Csonka, O. A. Vydrov, G. E. Scuseria, L. A. Constantin, X. Zhou, and K. Burke, *Phys. Rev. Lett.* **100**, 136406 (2008).
- [39] P. E. Blöchl, *Phys. Rev. B* **50**, 17953 (1994).
- [40] Y. Le Page and P. Saxe, *Phys. Rev. B* **65**, 104104 (2002).
- [41] B. Winchester, P. Wu, and L. Q. Chen, *Appl. Phys. Lett.* **99**, 052903 (2011).
- [42] R. Hull and J. C. Bean, *Crit. Rev. Solid State Mater. Sci.* **17**, 507 (1992).
- [43] V. Shelke, D. Mazumdar, S. Jesse, S. Kalinin, A. Baddorf, and A. Gupta, *New J. Phys.* **14**, 053040 (2012).
- [44] A. Umantsev, *Field Theoretic Method in Phase Transformations* (Springer, New York, Dordrecht, Heidelberg, London, 2012).
- [45] R. Indergand, A. Vidyasagar, N. Nadkarni, and D. M. Kochmann, *J. Mech. Phys. Solids* **144**, 104098 (2020).
- [46] A. Devonshire, *Adv. Phys.* **3**, 85 (1954).
- [47] J.-M. T. K. M. Rabe and C. H. Ahn, *Physics of Ferroelectrics. A Modern Perspective* (Springer, Berlin, Heidelberg, 2007).
- [48] F. Xue, Y. Gu, L. Liang, Y. Wang, and L.-Q. Chen, *Phys. Rev. B* **90**, 220101(R) (2014).
- [49] Q. Shi, E. Parsonnet, X. Cheng, N. Fedorova, R.-C. Peng, A. Fernandez, A. Qualls, X. Huang, X. Chang, H. Zhang *et al.*, *Nat. Commun.* **13**, 1110 (2022).
- [50] *Runge–Kutta Methods* (John Wiley and Sons, New York, 2016), Chap. 3, pp. 143–331.
- [51] D. Karpinsky, M. Silibin, D. Zhaludkevich, S. Latushka, A. Sysa, V. Sikolenko, A. Zhaludkevich, V. Khomchenko, A. Franz, K. Mazeika *et al.*, *J. Magn. Magn. Mater.* **539**, 168409 (2021).